### **ORIGINAL ARTICLE**



# Novel adaptive extended state observer method of active disturbance rejection control for sensorless IPMSMs based on high-frequency square wave injection

Liwei Wang 1,2 · Hong Miao<sup>2</sup>

Received: 4 January 2025 / Revised: 26 May 2025 / Accepted: 27 May 2025 © The Author(s) 2025

#### **Abstract**

The sensorless control method for built-in interior permanent magnet synchronous motors (IPMSMs) based on high-frequency square-wave (HF) injection is being increasingly applied in electric vehicles due to its compact size and low cost. However, sensorless IPMSMs have weak anti-interference capability and poor dynamic performance, especially at low speeds. A novel adaptive extended state observer (AESO) for the active disturbance rejection control (ADRC) of a sensorless IPMSM with HF square-wave injection is proposed. First, HF square-wave signals are injected into the estimated rotational coordinate system of the IPMSM, and the rotor position estimation error is obtained through signal response extraction and processing. Then, a novel AESO-based ADRC (AESO\_ADRC) is designed to replace the traditional PI controller in the speed loop. The characteristics of the AESO are obtained by allocating time-varying eigenvalues based on the differential algebraic spectrum theory (DAST) of the estimation errors of the rotor position, speed, and total disturbances to reduce the disturbance of the state estimation error and the total disturbance. Simulation and experimental results demonstrate that the stabilization time of the AESO\_ADRC method is the shortest under sudden changes in load and speed, with nearly zero overshoot. These results indicate that the AESO\_ADRC method has good dynamic performance and strong anti-interference capability. Moreover, the method performs well at low speeds of 10 r/min, and the rotor position estimation error is minimum.

 $\textbf{Keywords} \ \ IPMSM \cdot Position \ sensorless \ control \cdot High-frequency \ square-wave \ injection \cdot ADRC \cdot AESO$ 

### 1 Introduction

IPMSMs are widely used in electric vehicles and other fields due to their merits, such as compact structure, high power density, and wide speed range [1]. Sensorless control technology for IPMSMs is gradually replacing traditional sensor-based methods, because it reduces motor volume and cost while increasing the system reliability [2]. However, the high-performance control of IPMSMs is still extremely challenging, especially when the motor operates at low speeds. Modeling uncertainties, inverter nonlinearity, and

other factors result in low signal-to-noise ratio and external interference, which degrade its dynamic performance. Thus, developing control methods to improve the dynamic performance and anti-interference capability of sensorless IPMSM systems has become a research hotspot [3].

High-frequency signal injection has become an effective approach for sensorless control in the low-speed domain of IPMSM, due to its low sensitivity to motor parameters and good position estimation accuracy [4]. However, traditional methods of injecting high-frequency sine signals or high-frequency pulse signals require the use of a large number of filters in the signal processing, which increases system costs, limits the bandwidth, and reduces dynamic performance [5]. To overcome this weakness, the squarewave signal injection method, which increases the signal frequency, has been proposed [6, 7]. Therefore, this method increases the bandwidth of the controller and improves the robustness of the system [8, 9]. Nevertheless, there is still poor low-speed dynamic performance. Thus, most methods focus on improving injection signals for better results.

Published online: 24 June 2025



<sup>☐</sup> Liwei Wang wangliwei@scu.edu.cn; 24054976g@connect.polyu.hk

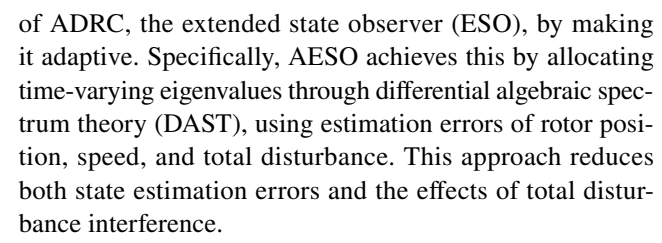
Department of Electrical and Electronic Engineering, The Hong Kong Polytechnic University, Kowloon, Hong Kong Special Administrative Region, China

College of the Electrical Engineering, Sichuan University, Chengdu, China

The authors of [10] used traditional high-frequency square-wave voltage injection (HFSVI) and high-frequency pulse voltage injection (HFPVI) [11], while the authors of [12] used adjustable high-frequency square-wave voltage injection. These methods have achieved certain improvements in dynamic performance at low speeds. However, due to uncertainty factors such as the lack of internal dynamic models and external disturbances, the control dynamic performance of the IPMSM may seriously deteriorate. To achieve high-performance control of IPMSM, it is necessary to further improve the dynamic performance and anti-interference capability of sensorless control [11].

Since ADRC does not rely on accurate mathematical models and has strong anti-interference capability, it is used for the control of high-frequency square-wave injection in position sensorless IPMSM. This method combines the unknown dynamics and external disturbances of the system into a total disturbance, which is represented by an extended state, that is estimated and compensated [13]. In the design of nonlinear ADRC of the IPMSM, due to its complex structure, a large number of parameters need to be adjusted, making it difficult to analyze the stability and estimation error [14]. To simplify the controller design, the authors of [15, 16] proposed a linearized active disturbance rejection control (LADRC) method, carried out a complete stability analysis of LADRC, and introduced a parameter adjustment method that only requires adjusting the bandwidth. The authors of [17, 18] designed a fuzzy linear active disturbance rejection control (Fuzzy-LADRC) based on IPMSM speed loop control with fuzzy linear active disturbance rejection control, resulting in smaller motor speed fluctuations. The authors of [19, 20] designed an active disturbance rejection controller (ADRC) for the current inner loop, which is independent of the permanent magnet flux linkage parameters. This method achieves good rotor position estimation and demonstrates excellent steady-state performance. The authors of [21] used ESO and NLEF of ADRC to estimate and compensate for nonlinear and uncertain disturbances. The authors of [22] proposed an extended state observer (LESO) that estimates position and speed while accounting for disturbance. However, ADRC may sacrifice its flexibility to improve performance. In addition, the larger observer gain may exceed its bandwidth. Furthermore, for the high gain observer, when the initial real state and the estimated state do not match, the oscillation peak phenomenon may occur. The IPMSM control based on ADRC still has state estimation errors and total disturbances, which affect the dynamic performance.

In this paper, to further enhance dynamic performance and anti-interference capability, a novel adaptive extended state observer (AESO) method is proposed for the active disturbance rejection control (ADRC) of sensorless IPMSMs using high-frequency (HF) square-wave injection. The key idea of AESO ADRC is to enhance the core component



First, a high-frequency square-wave is injected into the estimated rotating coordinate system, and the rotor position estimation error is obtained through signal extraction and processing. Then, an adaptive ESO based on the DAST in [17] is designed using the error signal to estimate the total disturbance and state variables of the system, obtain accurate rotor position information, and construct an AESO for the ADRC controller to replace the traditional PI controller in the speed loop. Finally, the effectiveness of the proposed method is verified through MATLAB/Simulink simulation results and experimental results.

### 2 Principle of high-frequency square-wave injection for position estimation

In the synchronous rotating coordinate system, when the IPMSM operates at low speed, the counter electromotive force and the voltage drop of the stator resistance can be ignored. The voltage equation of the IPMSM after injecting HF signals is expressed as Eq. (1) [9, 20].

$$\begin{bmatrix} u_{dh} \\ u_{dh} \end{bmatrix} = \begin{bmatrix} L_{dh} & 0 \\ 0 & L_{dh} \end{bmatrix} p \begin{bmatrix} i_{dh} \\ i_{dh} \end{bmatrix}, \tag{1}$$

where the subscript h represents the corresponding HF component. p is a differential operator.  $u_{dh}$  and  $u_{qh}$  are the HF stator voltage along the d- and q-axes, respectively.  $i_{dh}$  and  $i_{qh}$  are the HF stator currents along the d- and q-axes, respectively.  $L_{dh}$  and  $L_{qh}$  are the inductances along the d- and q-axes, respectively.

The HF square-wave voltage signals injected in the  $d^e$  axis of the estimated coordinate are described in (2) and (3).

$$u_{\rm inj} = \begin{bmatrix} u_{dh}^e \\ u_{qh}^e \end{bmatrix} = V_{\rm in} \begin{bmatrix} 1 \\ 0 \end{bmatrix}$$
 (2)

$$V_{\text{in}} = \begin{cases} V_h, t \in [2nT_s, (2n+1)T_s] \\ -V_h, t \in [(2n+1)T_s, (2n+2)T_s \end{cases}, \quad n = 0, 1 \dots (3)$$

where  $u_{inj}$  is the vector of the injected HF square wave in the estimated rotational coordinate system.  $u_{dh}^e$  and  $u_{qh}^e$  are the  $d^e$ - and  $q^e$ -axis stator voltages of the injected HF square wave.  $V_{in}$  represents the injected HF square wave. t is the time variable.  $T_s$  is the duration of the positive and negative



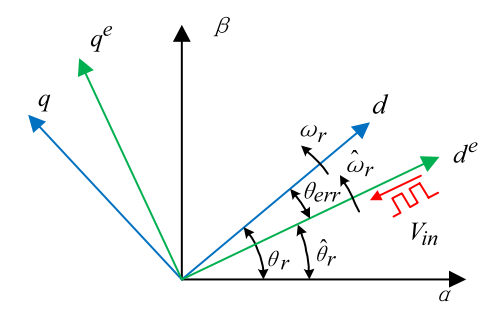


Fig. 1 Schematic diagram of HF square-wave signal injection

voltage,  $V_h$  is the amplitude of the injection voltage, and n is the number of sequences. The schematic diagram of the injected square-wave signal is shown in Fig. 1.

In Fig. 1,  $\alpha$  and  $\beta$  form a stationary coordinate system.  $\theta_{\rm err}$  is the error of the estimated rotor position, defined as  $\theta_{\rm err} = \theta_r - \hat{\theta}_r$ . In addition,  $\theta_r$  and  $\hat{\theta}_r$  are the actual and estimated values of the rotor position, respectively.  $\omega_r$  and  $\hat{\omega}_r$  are the actual and estimated values of the rotor angular velocity, respectively.

According to Eq. (1), when the HF square-wave signal is injected, the HF current responses in the stationary  $\alpha\beta$  coordinate system are  $\Delta i_{\alpha h}$  and  $\Delta i_{\beta h}$ , respectively

$$\begin{bmatrix} \Delta i_{\alpha h} \\ \Delta i_{\beta h} \end{bmatrix} = R^{-1} \begin{pmatrix} \theta_r \end{pmatrix} \begin{bmatrix} L_{dh} & 0 \\ 0 & L_{dh} \end{bmatrix}^{-1} R(\theta_{\text{err}}) \int u_{inj} dt, \qquad (4)$$

where the coordinate transformation matrix  $R(\theta_r)$  is represented by Eq. (5), and  $R(\theta_{\rm err})$  is the same transformation matrix.

$$R(\theta_r) = \begin{bmatrix} \cos(\theta_r) & \sin(\theta_r) \\ -\sin(\theta_r) & \cos(\theta_r) \end{bmatrix}. \tag{5}$$

The HF current response can be derived from (4)

$$\begin{bmatrix} \Delta i_{ah} \\ \Delta i_{\beta h} \end{bmatrix} = \frac{V_{in} \Delta T_s}{L_{dh} L_{qh}} \begin{bmatrix} L_{qh} \cos(\theta_r) \cos(\theta_{err}) + L_{dh} \sin(\theta_r) \sin(\theta_{err}) \\ L_{qh} \sin(\theta_r) \cos(\theta_{err}) - L_{dh} \cos(\theta_r) \sin(\theta_{err}) \end{bmatrix}. \tag{6}$$

When  $\theta_{\rm err}$  approaches 0, the envelope of the HF current response with rotor position information can be simplified from Eq. (6) to Eq. (7).  $\Delta i_{\alpha h}$  and  $\Delta i_{\beta h}$  are expressed by  $I_{\rm sin}$  and  $I_{\rm cos}$ 

$$\begin{bmatrix} I_{\sin} \\ I_{\cos} \end{bmatrix} = \begin{bmatrix} \Delta i_{\alpha h} \\ \Delta i_{\beta h} \end{bmatrix} \approx \frac{V_{in} \Delta T_s}{L_{dh}} \begin{bmatrix} \cos(\theta_r) \\ \sin(\theta_r) \end{bmatrix}. \tag{7}$$

From Eq. (7), rotor position information can be obtained by setting a suitable position observer. Figure 2 gives the demodulation block diagram of the position error signal

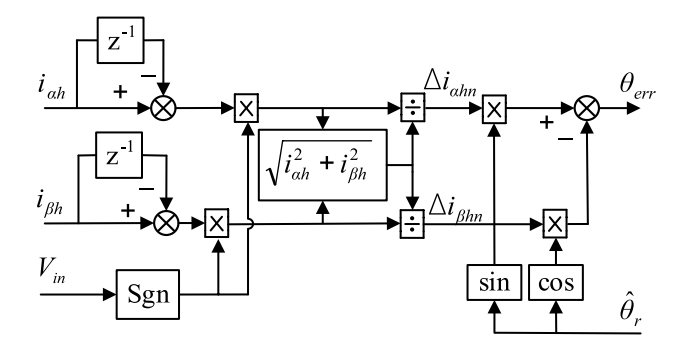


Fig. 2 Demodulation block diagram of the position error signal

of the high-frequency square-wave injection method [17]. Here, Sgn is a sign function

### 3 Novel adaptive extended state observer of ADRC

#### 3.1 IPMSM mathematical model with disturbance

In the dq synchronous rotating coordinate system, the electromagnetic torque equation of the IPMSM is expressed as [16]

$$T_e = \frac{3}{2} n_p \left[ \psi_f I_s \sin \gamma - \left( L_d - L_q \right) I_s^2 \sin \gamma \cos \gamma \right], \tag{8}$$

where  $T_{\rm e}$  is the electromagnetic torque,  $n_p$  is the number of poles of the IPMSM, and  $\psi_f$  is the magnetic flux of the permanent magnet.  $I_s$  is the amplitude of the stator current, and  $\gamma$  is the angle between the stator flux vector and the permanent magnet flux vector.  $L_d$  and  $L_q$  are the inductances along d- and q-axes, respectively.

Based on Eq. (8), the electrical angular velocity can be expressed as [16]

$$\dot{\omega}_r = \frac{n_p}{J} \left( T_e - T_L \right) - \frac{B}{J} \omega_r = b_0 I_s + f, \tag{9}$$

where B is the damping coefficient,  $T_L$  is the load torque, and J is the moment of inertia. f is the total disturbance, which is expressed as [16]

$$f = \frac{3}{2}n_p(L_d - L_q)I_s^2 \sin\gamma \cos\gamma - \frac{n_p}{J}T_L - \frac{B}{J}\omega_r - (b - b_0)I_s,$$
(10)

where

$$b = \frac{3}{2J} n_p^2 \psi_f I_s \sin\gamma \tag{11}$$



$$b_0 = \frac{3}{2\hat{J}} n_p^2 \hat{\psi}_f I_s \sin \hat{\gamma},\tag{12}$$

where b is the intermediate variable, and  $b_0$  is the compensation factor. The top mark  $\cdot$  indicates the first-order derivation, and the top mark  $^{\wedge}$  represents the estimated value. Thus, the equation of the state of the IPMSM is extended to Eq. (14)

$$\begin{cases} \dot{\theta}_r = \omega_r \\ \dot{\omega}_r = b_0 I_s + f \\ \dot{f} = h(x, w) \end{cases}$$
 (13)

Here, h(x,w) is an unknown and bounded function, which can be observed and compensated for.

### 3.2 ADRC controller

ADRC consists of a tracking differentiator (TD), a nonlinear state error feedback control law (NLSEF), an extended state observer (ESO), and a disturbance compensation. The structural schematic diagram of the second-order ADRC is shown in Fig. 3.

The reference signal generates the transition signal  $x_1$  and its differential signal  $x_2$  through TD. Comparing the transition signal and its differential signal with the system output feedback signal and its differential signal, the state errors  $e_1$  and  $e_2$  are generated. The state error is input into the NLSEF to generate a preliminary control signal  $u_0$ . The ESO estimates the system state and total disturbance in real time, and adds the disturbance compensation signal to the control signal  $u_0$ . The control signal acts on the controlled object to improve the control performance.

The tracking differentiator (TD) in ADRC quickly tracks input instructions and obtains differentiation of the tracking signal. Assuming the input signal is v(t), the discretization of the fastest tracking differentiator for second-order systems is (14)

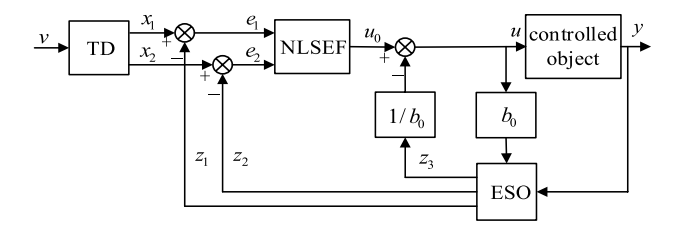


Fig. 3 Structure diagram of the ADRC controller

$$\underline{\underline{\mathscr{D}}}$$
 Springer

$$\begin{cases} e(k) = x_1(k) - v(k) \\ fh = fhan(e(k), x_2(k), r_0, h_0) \\ x_1(k+1) = x_1(k) + hx_2(k) \\ x_2(k+1) = x_2(k) + hfh \end{cases}$$
(14)

where k is the number of discretization iterations,  $x_1(k)$  is the k-th order discretization tracking signal of the input signal v(t),  $x_2(k)$  is the differential signal of the k-order discretization v(k) of the input signal v(t), and e(k) represents the k-th estimation error. The maximum of  $x_2$  differentiation is  $r_0$ , h is the sampling period,  $r_0$  is the speed factor, where the larger the value of  $r_0$ , the better its tracking performance.  $h_0$  is the filtering factor, and the larger the value of  $h_0$ , the stronger the noise filtering.  $r_0$  and  $h_0$  are both adjustable parameters. The function  $fhan(\cdot)$  is the fastest tracking synthesis function of a discrete system, expressed as (15)

$$fhan = -r_0 \left[ \frac{a}{d} - \operatorname{sign}(a) \right] s_a - r_0 \operatorname{sign}(a). \tag{15}$$

The intermediate variables are defined as follows:

$$\begin{cases} d = r_0 h_0^2 \\ a_0 = h_0 x_2 \\ y = x_1 + a_0 \\ a_1 = \sqrt{d(d+8|y|)} \\ a_2 = a_0 + 1/2 \operatorname{Sgn}(y)(a_1 - d) \\ s_y = 1/2 [\operatorname{Sgn}(y+d) - \operatorname{Sgn}(y-d)] \\ a = (a_0 + y - a_2) s_y + a_2 \\ s_a = 1/2 [\operatorname{Sgn}(a+d) - \operatorname{Sgn}(a-d)] \end{cases}$$
(16)

In addition, Sgn is a sign function, which is defined as: when t > 0, Sgn t = 1; when t = 0, Sgn t = 0; when t < 0, Sgn t = -1.

The ESO algorithm is shown in Eq. (17)

$$\begin{cases} \varepsilon = z_1 - y \\ \dot{z}_1 = z_2 - \beta_{01} fal(\varepsilon, a_1, \delta) \\ \dot{z}_2 = z_3 - \beta_{02} fal(\varepsilon, a_2, \delta) + f_0(z_1, z_2) + b_0 u' \\ \dot{z}_3 = -\beta_{03} fal(\varepsilon, a_3, \delta) \end{cases}$$

$$(17)$$

where  $fal(\cdot)$  is a nonlinear function, represented by (18)

$$fal(\varepsilon, a, \delta) = \begin{cases} \varepsilon / \delta^{(1-a)}, |\varepsilon| \le \delta \\ \operatorname{Sgn}(\varepsilon) |\varepsilon|^{a}, |\varepsilon| > \delta \end{cases}$$
(18)

where  $\varepsilon$  is the error between the output of the controlled object and its observed value. The output signals  $z_1$ ,  $z_2$ , and  $z_3$  of the ESO are the estimated output values of the system, its estimated output differential values, and the estimated

total disturbance values, respectively.  $\beta_{01}$ ,  $\beta_{02}$ , and  $\beta_{03}$  are the observer gain of the ESO, and  $\delta$  is the filtering factor. u is the input, and  $f_0$  is disturbance.

The input of nonlinear state error feedback control (NLSEF) is the error of the TD output tracking signal  $x_1$  and the tracking differential signal  $x_2$  with ESO estimated signals  $z_1$  and  $z_2$ , respectively. The algorithm is as follows:

$$u_0 = \beta_1 fal(e_{01}, a_4, \delta_0) + \beta_2 fal(e_{02}, a_5, \delta_0), \tag{19}$$

where  $u_0$  is the control variable of the controller,  $\beta_1$  and  $\beta_2$  are the proportional gains,  $e_{01}$  and  $e_{02}$  are the output and observation errors of the control objects of the two nonlinear functions  $fa(\cdot)$  in Eq. (19),  $a_4$  and  $a_5$  are the powers of the two nonlinear functions  $fal(\cdot)$ , and  $\delta_0$  is the filtering factor.

Based on the disturbance estimation signal output by the ESO and the known part of the controlled object, the compensation process for disturbances can be obtained as Eq. (20)

$$u = u_0 - z_3 / b_0, (20)$$

where u is the input signal of the controlled object, and  $b_0$  is the compensation factor.

### 3.3 Design of the adaptive extended state observer

According to Eq. (17), the adaptive extended state observer (AESO) can be designed as (20)

$$\begin{cases} \dot{e}_{1} = \theta_{r} - \theta_{r} \\ \dot{\theta}_{r} = \hat{\omega}_{r} - l_{1}(t) \cdot m_{1}(e_{1}) \\ \dot{\hat{\omega}}_{r} = \hat{f} + b_{0}l_{s} - l_{2}(t) \cdot m_{2}(e_{1}) \\ \dot{\hat{f}} = -l_{3}(t) \cdot m_{3}(e_{1}) \end{cases}$$
(21)

where  $e_1$ ,  $e_2$ , and  $e_3$  are the estimation errors of the rotor position, speed, and total disturbance, which can be defined as  $e_1 = \hat{\theta}_r - \theta_r$ ,  $e_2 = \hat{\omega}_r - \omega_r$ , and  $e_3 = \hat{f} - f$ , respectively. Thus, a third-order error dynamic equation can be derived as Eq. (22)

$$\begin{cases} \dot{e}_1 = e_2 - l_1(t) \cdot m_1(e_1) \\ \dot{e}_2 = e_3 - l_2(t) \cdot m_2(e_1) \\ \dot{e}_3 = -l_3(t) \cdot m_3(e_1) - h(x, w) \end{cases}$$
(22)

where  $m_i(e_1)$  is a  $fal(\cdot)$  function,  $l_1(t)$ ,  $l_2(t)$ , and  $l_3(t)$  are nonlinear functions. According to differential algebraic spectrum theory (DAST), time-varying eigenvalues are allocated to achieve adaptive characteristics, thereby reducing the state estimation errors and the total disturbance interference. In the improved adaptive AESO,  $m_i(e_1) = e_1$  is selected.

Based on Eq. (22), the state space of the error dynamic equation can be described as

$$\dot{e} = A_c(t)e - B_e h(x, w), \tag{23}$$

where 
$$\mathbf{e} = [e_1, e_2, e_3]^T$$
,  $A(t) = \begin{bmatrix} -l_1(t) & 1 & 0 \\ -l_2(t) & 0 & 1 \\ -l_3(t) & 0 & 0 \end{bmatrix}$ , and  $\mathbf{B}_c = \begin{bmatrix} -l_1(t) & 1 & 0 \\ -l_2(t) & 0 & 1 \\ -l_3(t) & 0 & 0 \end{bmatrix}$ 

 $[0,0,1]^T$ ; x is the state variable, and w is the external disturbance.

**Definition**: The observer gain matrix is  $L(t) = [-l_1(t), -l_2(t), -l_3(t)]^T$ . Equation (23) is a controllable linear timevarying (LTV) system with unknown but bounded inputs. The gain matrix A(t) is designed to ensure the stability of Eq. (23) and to achieve good estimation performance. First, the AESO error dynamic equation is converted to standard form using a Lyapunov transformation, as shown in Eq. (24)

$$\dot{z} = A_c(t) - B_c h(x, w), \tag{24}$$

where 
$$A_c(t) = \begin{bmatrix} 0 & 0 & 0 \\ 0 & 0 & 0 \\ -g_1(t) & -g_2(t) & -g_3(t) \end{bmatrix}, \boldsymbol{B}_c = [0,0,1]^{\mathrm{T}}.$$

The controllable standard form (24) is an implementation of a linear scalar differential system described by Eq. (25), where the elements in  $A_c(t)$  are the coefficients of the equation. Here,  $\xi$  represents the variables of a linear system

$$\xi^{(3)} + g_3(t)\xi^{(2)} + g_2(t)\dot{\xi} + g_1(t)\xi = B_c(-h(x,w)), \tag{25}$$

where the superscript (3), (2), and  $\cdot$  represent the third, second, and first derivatives, respectively.

The observer gain matrix L(t) can be transformed into

$$L(t) = \left[ -g_3(t), -\left(g_2(t) - 2\dot{g}_3(t)\right), -\left(g_1(t) + g_3^{(2)}(t) - \dot{g}_2(t)\right) \right]^{\mathrm{T}}. \tag{26}$$

The observer gain  $l_i(t)$  is designed to be converted into a time-varying parameter  $g_i(t)$  to stabilize the AESO and maximize its performance. The homogeneous equation of the linear scalar differential Eq. (25) is expressed as

$$\xi^{(3)} + g_3(t)\xi^{(2)} + g_2(t)\dot{\xi} + g_1(t) = 0. \tag{27}$$

Using the scalar polynomial differential operator (SPDO), the LTV system (27) is represented as  $\mathcal{D}_a\{\xi\}=0$ , as shown in Eq. (28)

$$D_a = \delta^{(3)} + g_3(t)\delta^{(2)} + g_2(t)\delta + g_1(t), \tag{28}$$

where  $\delta = \mathrm{d}/\mathrm{d}t$  is the derivative operator, and  $\mathcal{D}_a$  represents the scalar polynomial differential operator. The unified general theory of the LTV is established through the classical factorization of the SPDO with the Floquet theory. Floquet factorization is

$$D_a = \left(\delta - \lambda_3(t)\right) \left(\delta - \lambda_2(t)\right) \left(\delta - \lambda_1(t)\right). \tag{29}$$



In the unified spectrum theory, the set  $\{\lambda_i(t)\}_{k=1}^n$  in Eq. (29) is called the SD spectrum of  $D_a(\xi)$ . The set  $\{\rho(t) = \lambda_{1,k}(t)\}_{k=1}^n$  is called the PD spectrum of  $D_a(\xi)$ , where  $\lambda_{1,k}(t)$  denotes n special solutions of  $\lambda_1(t)$  that satisfies certain nonlinear independent constraints.  $A_c(t)$  is referred to as the companion matrix associated with  $D_a$ . The diagonal matrix diag $[(\rho_1(t), \rho_1(t), \rho_1(t)]$  is called the standard form of the parallel spectrum (PD) of  $D_a$  and  $A_c(t)$ .

The companion matrix  $A_c(t)$  is simplified to its related canonical form  $\eta(t)$  by the transformation matrix V(t), and  $\eta(t)$  can be given as

$$\eta(t) = V^{-1}(t) \left[ A_c(t) V(t) - \dot{V}(t) \right]. \tag{30}$$

To calculate  $g_i(t)$  through  $\rho_i(t)$ , the following two theorems are introduced.

**Theorem 1**: Let  $\{\rho_i(t)\}_{i=1}^p$  be the PD spectrum of the order p SPDO( $D_a$ ), and let  $V_k(t)$  be the determinant of the k-th order transformation arrive in Eq. (30). Then, the SD spectrum of  $D_a$ , i.e.  $\{\lambda_i(t)\}_{i=1}^p$  is obtained

$$\lambda_k(t) = \rho_k(t) + \dot{V}_k(t) / V_k(t) - \dot{V}_{k-1}(t) / V_{k-1}(t), \tag{31}$$

where j = 1, ..., p and  $V_0(t) = 1$ .

**Theorem 2:** Let  $\left\{\lambda_i(t)\right\}_{i=1}^p$  be the SD spectrum of the order p SPDO $(D_a)$ , and let the p coefficients of  $D_a$  be defined as  $g_{p,j}(t)$ ,  $g_{k,0}(t)=0$ , and  $g_{k,k+1}(t)=1$ . Then,  $g_{p,j}(t)$  can be recursively calculated as

$$g_{p,j}(t) = \dot{g}_{p-1,j}(t) - \lambda_{p} g_{p-1,j}(t) + g_{p-1,j-1}(t), \tag{32}$$

where j = 1,...,p and k = 1,...,p-1. Let y be the SD spectrum of the order-p spdo(f).

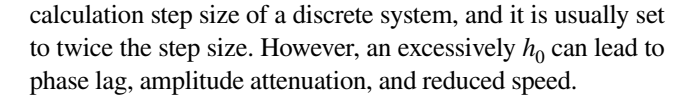
According to theorems 1 and 2,  $g_i(t)$  can be obtained by allocating appropriate eigenvalues  $\rho_i(t)$ .

### 3.4 Parameter design of the AESO ADRC

The parameters that need to be designed and adjusted in this paper include the relevant parameters of TD, AESO, and NLSEF.

### (1) Design of TD parameters

The parameters of TD include the velocity factor  $r_0$  and the filtering factor  $h_0$ .  $r_0$  determines the tracking speed of the signal. The larger  $r_0$  is, the faster the transition process is tracked, the smaller the phase lag, and the smaller the amplitude attenuation, resulting in a closer approximation to the true value. However, due to the limitations of the physical characteristics and control variables of the controlled object,  $r_0$  cannot be too large, because an excessively large  $r_0$  may exacerbate oscillation. An appropriate value of  $h_0$  can eliminate overshoot and reduce the static error. Generally,  $h_0$  should be larger than the



#### (2) Design of the conventional ESO parameters

Conventional parameters include  $\beta_{01}$ ,  $\beta_{02}$ ,  $\beta_{03}$ ,  $a_1$ ,  $a_2$ ,  $a_3$ , and  $\delta$ . Usually,  $a_1$ ,  $a_2$ ,  $a_3$ , and  $\delta$  are designed as fixed parameters. If  $0 < a_i \le 1$  (i = 1, 2, 3), the smaller  $a_i$ , the better the tracking effect. In this section,  $a_1 = 0.75$ ,  $a_2 = 0.5$ , and  $a_3 = 0.5$ 0.25.  $\delta$  is the filtering factor, and the larger the value of  $\delta$ , the better the filtering effect. However, this also increases the tracking delay. Generally,  $\delta$  should be within the range of [5] T, 10 T], where T is the sampling period. In this section,  $\delta$ = 0.01 is selected [13]. The observer gain  $\beta_{01}$ ,  $\beta_{02}$ , and  $\beta_{03}$  need to be set, and their values determine the estimation accuracy of the observer. The other observer parameters are tuned and simplified to a tuning optimization of  $\omega_0$  [12], i.e.,  $\beta_{01} = 3\omega_0$ ,  $\beta_{02} = 3\omega_0^2$ , and  $\beta_{03} = \omega_0^3$ .  $\omega_0$  should be maximized as much as possible within the allowable range of noise sensitivity and sampling delay. Excessive  $\beta_{01}$  can lead to oscillation or even divergence.  $\beta_{01}$  is usually on the same order of magnitude as 1/h. If  $\beta_{02}$  is too small, it can cause divergence; if it is too large, it can introduce high-frequency noise. If  $\beta_{03}$  is too small, it can reduce the tracking speed; and if  $\beta_{03}$  is too large, it can cause oscillation.

### (3) Design of the AESO parameters

According to the analysis of AESO in Sect. 3.3 of this paper, the observer gains  $l_1(t)$  to  $l_3(t)$  are designed as the time-varying parameters  $g_1(t)$  to  $g_3(t)$  to stabilize AESO and maximize its performance. Based on differential algebraic spectrum theory, time-varying eigenvalues are allocated to obtain adaptive characteristics. This is done to reduce the estimation errors of the states and the interference from the total disturbances.

The observer gains  $l_1(t)$  to  $l_3(t)$  are obtained by setting the eigenvalues as shown in Eq. (33)

$$\rho_i(t) = \overline{\rho}_i \omega(t), i = 1, 2, 3, \tag{33}$$

where  $\overline{\rho}_i$  represents the reference eigenvalues, and  $\omega(t)$  is a time-varying multiplier. The nominal eigenvalues are selected as  $\overline{\rho}_1 = -\omega_0$  and  $\overline{\rho}_{2,3} = -(-0.5 \pm j0.866)\omega_0$  to obtain the time-varying bandwidth  $\omega_n(t) = \omega_0\omega(t)$  of AESO. From Eqs. (31) and (32), it is obtained that

$$\begin{cases} g_{1}(t) = -\left(\overline{\rho}_{1}\overline{\rho}_{2}\overline{\rho}_{3}\right)\omega^{3}(t) \\ g_{2}(t) = \left(\overline{\rho}_{1}\overline{\rho}_{2} + \overline{\rho}_{1}\overline{\rho}_{3} + \overline{\rho}_{2}\overline{\rho}_{2}\right)\omega^{2}(t) + \left(\overline{\rho}_{1} + \overline{\rho}_{2} + \overline{\rho}_{2}\right)\dot{\omega}(t) \\ -\omega^{(2)}(t)/\omega(t) + \dot{\omega}^{2}(t)/\omega^{2}(t) \\ g_{3}(t) = \left(\overline{\rho}_{1} + \overline{\rho}_{2} + \overline{\rho}_{2}\right)(t) - \dot{\omega}(t)/\omega(t) \end{cases}$$

$$(34)$$



By defining a time-based function, the multiplier  $\omega(t)$  is designed as shown in Eq. (35)

$$\omega(t) = \begin{cases} \omega_0 / 3, t \le T_{\omega}, \\ \omega_0, t > T_{\omega}, \end{cases}$$
 (35)

 $\omega(t)$  and its derivative are generated by a Butterworth filter with  $\omega(t)$  as the input to the filter. When  $t \le T_{\omega}$ ,  $\omega(t)$  is set to  $\omega_0/3$ ; when  $t > T_{\omega}$ ,  $\omega(t)$  is set to  $\omega_0$ , which is beneficial for resolving conflicts between the speed and the overshoot.  $T_{\omega}$  is the time constant of the ESO.

#### (4) Design of the NLSEF parameters

The parameters of the NLSEF include  $\beta_1$ ,  $\beta_2$ ,  $a_4$ ,  $a_5$ , and  $\delta_0$ . For linear SEF, the parameters that need to be tuned are  $\beta_1$  and  $\beta_2$ , which are equivalent to the proportional gain  $K_p$  and the differential gain  $K_d$  by the PD control. For NLSEF, the selection of the parameters  $\beta_1$  and  $\beta_2$  is similar to that of the linear SEF. To avoid the speed fluctuations caused by an excessive gain,  $a_4$  is generally smaller than  $a_5$ , with  $0 \le a_4 \le 1 \le a_5$ . Typically,  $a_4 = 0.25$  and  $a_5 = 1.5$ .  $\delta_0$  is a parameter related to the range and control accuracy of the controlled quantity, and is usually set to  $\delta_0 = 0.22$  [22].

### (5) Design of the compensation parameters for disturbances

 $b_0$  is the compensation factor, an estimated value of the compensation coefficient, which is an important parameter affecting system stability. The selection of  $b_0$  should be a compromise between stability and response speed. Within a certain range, increasing  $b_0$  also increases the stability domain of the system. However, an excessively large  $b_0$  causes the control signal to be too small, resulting in a slower system response. The smaller the value of  $b_0$ , the faster the disturbance compensation response and the better the dynamic performance of the IPMSM. However, too small a  $b_0$  can cause overshoot and fluctuations.

In summary, the control block diagram of AESO\_ADRC for a position sensorless IPMSM based on HP square-wave injection is shown in Fig. 4. Rotor position information is extracted through high-frequency signal injection and signal processing. Combined with the real-time state estimation and disturbance compensation of ESO and the nonlinear control law of NLSEF, high-precision and strong robustness control of the IPMSM is realized. Figure 5 shows the structural diagram of AESO\_ADRC. The speed reference signal  $\omega_{r-ref}$  generates the transition signal  $\omega_{r1}$  and the differential signal  $\dot{\omega}_{r1}$  through TD. AESO obtains the rotor position estimate  $\hat{\theta}_r$ , the speed estimate  $\hat{\omega}_r = \dot{\theta}$ , and the total disturbance estimate  $\hat{f}$ . Through the

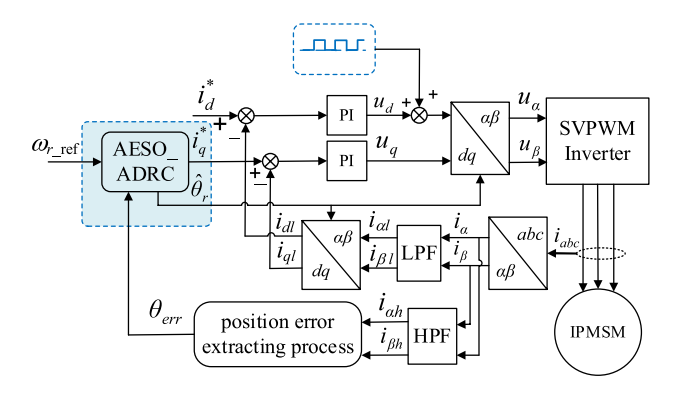


**Fig. 4** Control block diagram of AESO\_ADRC for a sensorless IPMSM based on HP square-wave injection

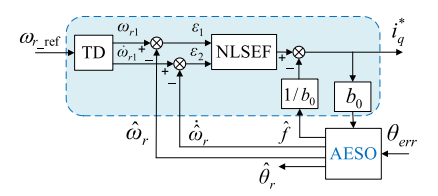


Fig. 5 Schematic diagram of AESO\_ADRC

differential algebraic spectrum theory (DAST), time-varying eigenvalues are allocated to optimize the dynamic response and estimation accuracy of the observer. The NLSEF generates the control signal  $i_a^*$  based on the error.

### 4 Simulation verification and analysis

To verify the effectiveness and feasibility of the novel control strategy proposed in this paper, simulation verification and analysis were conducted. A sensorless control system for an IPMSM based on LADRC, NADRC, and AESO\_ADRC controllers was built on the MATLAB/Simulink platform. The simulation parameters of the IPMSM are shown in Table 1. In the simulation, the switching frequency of the PWM is 10 kHz, and the dead time is set to 2.0  $\mu s$ . The current sampling frequency is the same as the PWM switching frequency. The injected HF square-wave voltage signal has a frequency of 5 kHz and an amplitude of 20 V.

The parameters of each part of the ADRC controller are selected as follows.

Sampling step size: h = 0.01.

Transition process parameters:  $r_0 = 20,000$ .

Nonlinear state error feedback parameters:

$$\beta_1 = 1.0, \beta_2 = 1.5, a_4 = 0.25, \text{ and } a_5 = 1.5, \delta_0 = 0.22.$$

LESO parameters:  $\beta_{01} = 100$ ,  $\beta_{02} = 30,000$ , and  $\beta_{03} = 10^6$ .



Table 1 IPMSM parameters

Parameter	Value
Phase number <i>m</i>	3
Number of pole pairs $n_p$	4
Rated speed r/min	1500
Rated power/kW	2.2
Stator phase resistance $R_s/m\Omega$	958
Direct inductance $L_d$ /mH	1.23
Quadratic inductance $L_q$ /mH	5.25
DC side voltage $U_d/V$	500

NESO parameters:  $\beta_{01} = 100$ ,  $\beta_{02} = 30,000$ ,  $\beta_{03} = 10^6$ ,  $a_1 = 0.75$ ,  $a_2 = 0.5$ ,  $a_3 = 0.25$ , and  $\delta = 0.01$ .

Disturbance compensation parameters:  $b_0 = 0.5b$ .

To compare and analyze the dynamic performance and anti-interference performance of LADRC, NADRC, AESO\_ADRC, and the traditional PI, simulation results were analyzed under different operating conditions and external disturbances of the IPMSM.

## 4.1 Comparison of dynamic performance during sudden load torque changes with the addition of random disturbances

As shown in Fig. 6a–d, the waveforms of the speed and stator current of the four control methods of the IPMSM are presented when the load torque suddenly increases from 0 to 20 Nm at 0.2 s and then suddenly decreases to 10 Nm at 0.4 s, under a given speed of 200 r/min and a random disturbance.

As shown in Fig. 6, when the load torque suddenly increases from 0 to 20 N·m at 0.2 s, the settling times of LADRC, NADRC, AESO\_ADRC, and the traditional PI control methods for the IPMSM are 0.022 s, 0.018 s, 0.012 s, and 0.1 s, respectively. When the load torque suddenly decreases at 0.4 s, the stabilization times are 0.0032 s, 0.0074 s, 0.0010 s, and 0.08 s, respectively. At 0.4 s, the load torque suddenly decreased from 20 to 10, and the settling times of the four control methods are 0.0032 s, 0.0074 s, 0.0010 s, and 0.08 s, respectively. Additionally, when the load is suddenly increased or decreased, the traditional PI overshoot is the largest, while the AESO\_ADRC overshoot is the smallest.

Thus, the method proposed in this paper demonstrates the shortest stability time during sudden load changes, near-zero overshoot, good dynamic performance, and strong anti-interference ability.

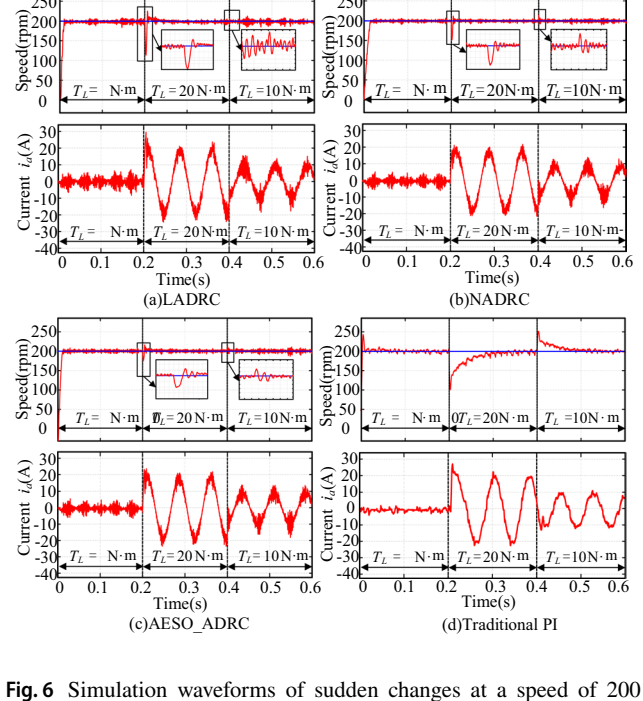


**Fig. 6** Simulation waveforms of sudden changes at a speed of 200 rpm and given torque values of 0, 20, and 10 Nm

## 4.2 Comparison of dynamic performance during sudden velocity changes with the addition of random disturbances

As shown in Fig. 7a–d, the waveforms of the speed and stator current of the four control methods of the IPMSM are presented when the speed suddenly increases from 10 to 200 r/min at 0.3 s and then suddenly decreases to 100 r/min at 0.6 s, under a given torque of 15 N·m with a random disturbance.

As shown in Fig. 7, at 0.3 s, the speed suddenly increases from 10 r/min to 200 r/min, the settling times of LADRC, NADRC, AESO\_ADRC, and the traditional PI control methods for the IPMSM are 0.012 s, 0.016 s, 0.014 s, and 0.335 s, respectively. At 0.6 s, the speed suddenly decreases from 200 r/min to 100 r/min, and the settling times of LADRC, NADRC, AESO\_ADRC, and the traditional PI control methods are 0.009 s, 0.014 s, 0.009 s, and 0.01 s, respectively. Additionally, NADRC and AESO\_ADRC have almost no overshoot, LADRC has a small amount of overshoot, and the traditional PI has a large overshoot. At the same time, it can be seen that AESO\_ADRC has good performance at a low speed of 10 r/min.

Therefore, the method proposed in this paper has the shortest stability time during sudden speed changes, which exhibits near-zero overshoot, possesses good dynamic performance, and strong anti-interference ability. At the same time, the proposed method performs well at low speeds.



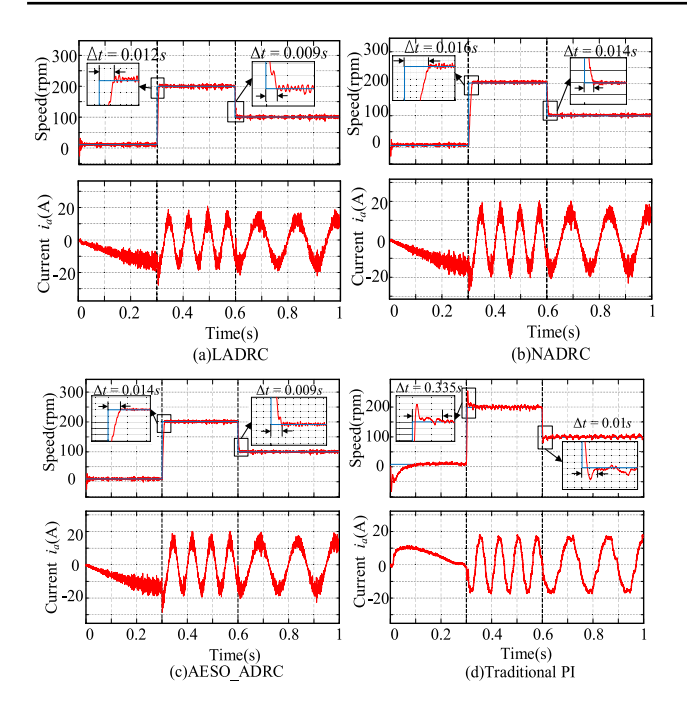


Fig. 7 Simulation waveform of sudden changes at a torque of 15 Nm and given speeds of 10, 200, and 100 rpm

## 4.3 Comparison of rotor position estimation accuracy with sudden load changes under external random disturbance

As shown in Fig. 8a–d, the rotor position estimation accuracies of the sensorless control methods for the IPMSM are compared under variable load torque conditions using LADRC, NADRC, AESO ADRC, and the traditional PI.

Given a speed of 200 r/min, under the condition of external limiting random disturbance, the load torque increases from 0 to 20 Nm at 2 s and decreases from 20 to 10 Nm at 4 s. After reaching a steady state, the maximum errors

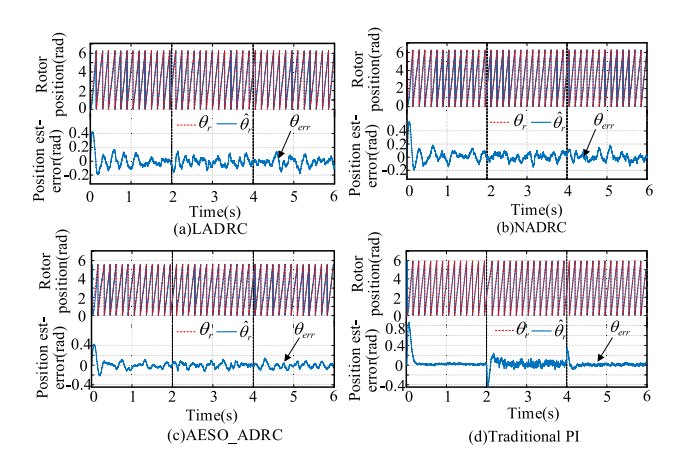


Fig. 8 Rotor estimation accuracy under sudden changes in the torque value of 0, 20, and 10 Nm at a speed of 200 r/min

in the rotor position estimation for LADRC, NADRC, and AESO\_ADRC are 0.18 rad/s, 0.2 rad/s, and 0.17 rad/s, respectively.

It can be observed that the rotor position estimation accuracy of AESO\_ADRC is higher than the other two ADRC methods, while the traditional PI control method has the highest rotor position estimation accuracy among the four methods when the load suddenly changes.

## 4.4 Comparison of rotor position estimation accuracy with speed variation under external random disturbance

As shown in Fig. 9a–d, the rotor position and position estimation error waveforms of the IPMSM sensorless control methods using LADRC, NADRC, AESO\_ADRC, and the traditional PI, with a given torque of 15 Nm and a random external disturbance, where the speed command increases from 20 to 200 r/min at 2 s and decreases from 200 to 100 r/min at 4 s, are presented.

As shown in Fig. 8a–d, the rotor position and position estimation error waveforms of the IPMSM sensorless control methods using LADRC, NADRC, AESO\_ADRC, and the traditional PI, with a given torque of 15 Nm and a random external disturbance, where the speed command increases from 20 to 200 r/min at 2 s and decreases from 200 to 100 r/min at 4 s, are presented.

At the steady state, the maximum estimation errors of the rotor position estimation for LADRC, NADRC, AESO\_ADRC, and the traditional PI are 0.165 rad/s, 0.200 rad/s, 0.1 rad/s, and 0.12 rad/s, respectively. It can be seen that the AESO\_ADRC method achieves the highest rotor position estimation accuracy and its rotor position estimation error is the smallest during low-speed sudden changes.

It can be concluded that under sudden changes in the load torque and speed, the AESO\_ADRC proposed in this

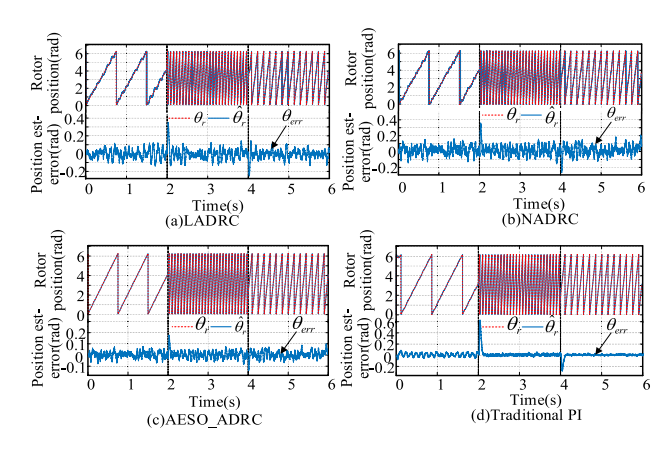


Fig. 9 Rotor estimation accuracy under sudden changes at a torque of 15 N·m and given speeds of 20 r/min, 200 r/min, and 100 r/min



paper has better dynamic performance, faster tracking speed, strong anti-interference ability, and good performance at low speeds compared to LADRC, NADRC, and PI control in the position sensorless control method of the IPMSM based on HF square-wave injection. Compared with the traditional PI, AESO\_ADRC has fewer dynamic position estimation errors. Additionally, AESO\_ADRC has higher position estimation accuracy than LADRC and NADRC.

### 5 Experimental verification and analysis

Figure 10 shows the experimental platform of a 2.2 kW IPMSM drive system driven by an inverter built in the laboratory. The parameters of the IPMSM are roughly the same as those listed in Table 1. The differences are as following: the stator phase resistance  $R_s$  is 839 m $\Omega$ , the direct inductance  $L_d$  is 5.05 mH, the quadratic inductance  $L_q$  is 15.35 mH, and the moment of inertia J is 0.00376 kg·m<sup>2</sup>.

### 5.1 Operating conditions with sudden load torque changes

To verify the dynamic performance of the load torque variation and the accuracy of the rotor position estimation, experiments were conducted under the conditions of a constant speed and variable load torque.

As shown in Figs. 11 and 12, when the load suddenly changes, the estimated rotor position is basically consistent with the actual value, and the steady-state position estimation error is within the range of 0.2 rad. The IPMSM speed has short-term fluctuations. It can be observed that the proposed control algorithm has good dynamic performance and accurate rotor position estimation under sudden load torque changes.

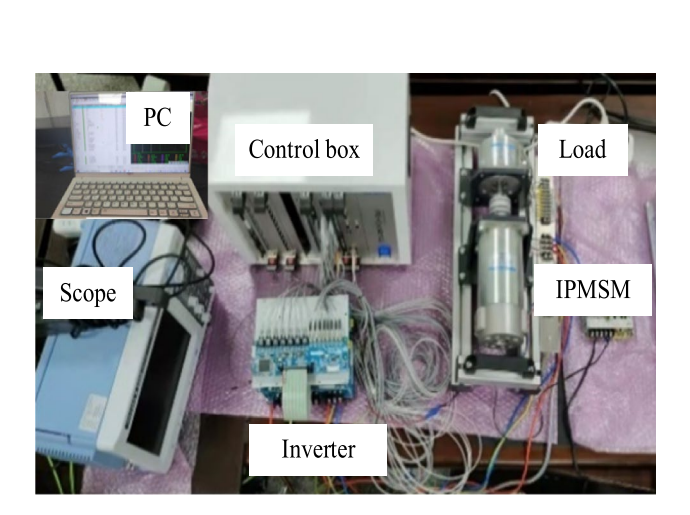


Fig. 10 Experimental platform of a 2.2 kW IPMSM drive



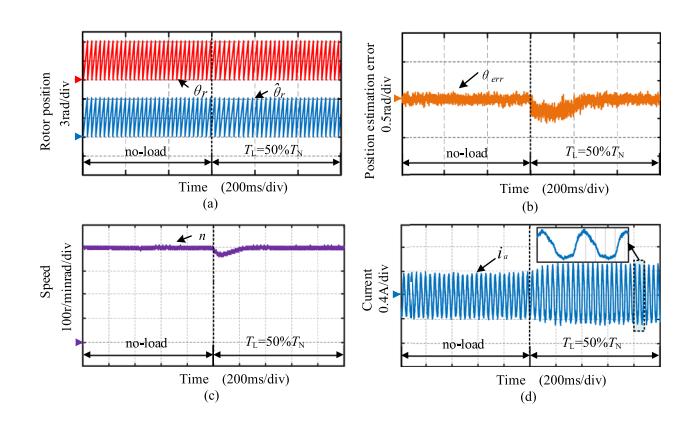


Fig. 11 Experimental results of a load torque increases from 0 to 50%  $T_{\rm N}$  at a speed of 400 r/min

### 5.2 Operating conditions with sudden speed changes

To verify the dynamic performance and accuracy of the rotor position estimation during speed changes, experimental verification was conducted under conditions of constant load and sudden speed changes.

As shown in Figs. 12 and 13, when the speed suddenly changes, the estimated rotor position is basically consistent with the actual value, and the maximum position estimation error is within the range of 0.2 rad. The IPMSM speed has short-term fluctuations (Fig. 14).

It can be seen that the control algorithm proposed in this paper has good dynamic performance and accurate rotor position estimation under speed changes.

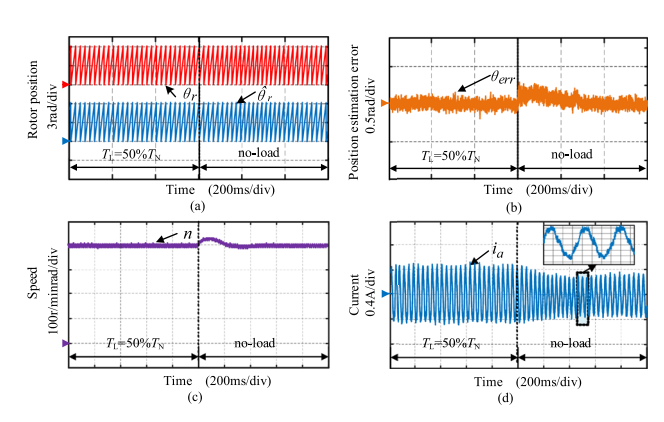


Fig. 12 Experimental results of a load torque drop from 50% to 0  $T_{\rm N}$  at a speed of 400 r/min

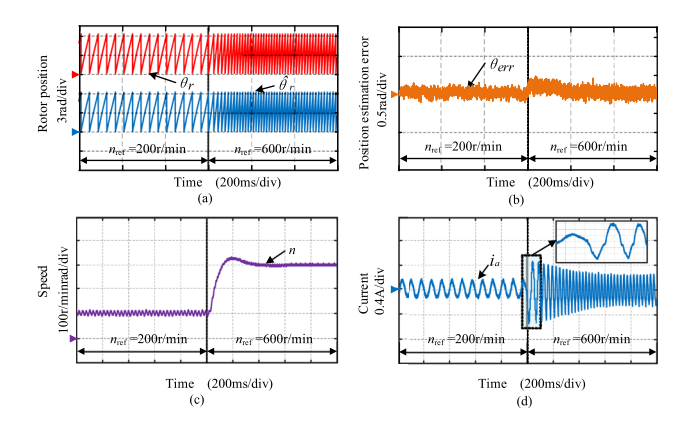


Fig. 13 Experimental results of a speed increase from 200 r/min to 600 r/min at a load torque of 50%  $T_{\rm N}$ 

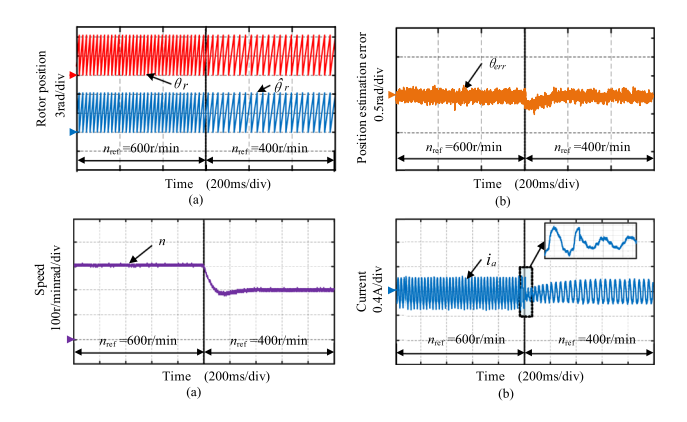


Fig. 14 Experimental results of a speed reduction from 600 r/min to 400 r/min at a load torque of 50%  $T_{\rm N}$ 

#### 6 Conclusion and further work

This paper proposed a novel adaptive ESO method for the active disturbance rejection control (AESO\_ADRC) of position sensorless IPMSMs based on high-frequency square-wave injection. The proposed method can solve the problem of poor dynamics and the weak anti-interference performance of sensorless IPMSMs, especially at low speeds. The main work and contributions of this paper are as follows:

First, high-frequency square waves are injected into the estimated rotational coordinate system of an IPMSM, and the estimation error of rotor position is obtained through the extraction and processing of injected signals and their responses.

Second, an adaptive extended state observer AESO based on the differential algebraic spectrum theory is designed using error signals, which estimate the total disturbance and state variables of the system to obtain accurate rotor position information. When the load torque

and speed suddenly change, the AESO\_ADRC has smaller dynamic position estimation errors than PI control. The AESO\_ADRC has a higher position estimation accuracy compared with LADRC and NADRC. Furthermore, during low-speed sudden changes, the rotor position estimation error is minimized.

Finally, the novel AESO\_ADRC with an adaptive extended state observer replaces the traditional PI controller in the speed loop. Under sudden changes in the load torque and speed, under random disturbances, the AESO\_ADRC proposed in this paper has better dynamic performance, faster tracking speed, stronger anti-interference ability, and better performance at low speeds than LADRC, NADRC, and PI control.

Due to limitations in the experimental conditions, the experimental process did not fully correspond to the simulation. In addition, the parameters design the AESO-ADRC which does not provide clear rules for parameter adjustment. To achieve better dynamic performance, the next step is to study the relevant parameter adjusting rules and improve the experiments.

**Acknowledgements** The authors thank the supports of Sichuan Science and Technology Program/2023YFG0198.

**Funding** Open access funding provided by The Hong Kong Polytechnic University. The work of Hong MIAO was funded by Sichuan Science and Technology Program, under Grant No. 2023YFG0198.

### **Declarations**

**Competing interest** The authors declare that they have no known competing financial interests or personal relationships that could have appeared to influence the work reported in this paper.

Open Access This article is licensed under a Creative Commons Attribution 4.0 International License, which permits use, sharing, adaptation, distribution and reproduction in any medium or format, as long as you give appropriate credit to the original author(s) and the source, provide a link to the Creative Commons licence, and indicate if changes were made. The images or other third party material in this article are included in the article's Creative Commons licence, unless indicated otherwise in a credit line to the material. If material is not included in the article's Creative Commons licence and your intended use is not permitted by statutory regulation or exceeds the permitted use, you will need to obtain permission directly from the copyright holder. To view a copy of this licence, visit http://creativecommons.org/licenses/by/4.0/.

### References

 Sardar, M.U., Manfeng, D., Saleem, U., Nawaz, M.K., Hassan, M.: A scholarly review of methods for design optimization of IPM synchronous motors used in electric vehicles. In: 2022 International Conference on Emerging Trends in Electrical, Control, and Telecommunication Engineering (ETECTE), Lahore, Pakistan, 2022, pp. 1–6. https://doi.org/10.1109/ETECTE55893.2022. 10007183



- Wang, G., Valla, M., Solsona, J.: Position sensorless permanent magnet synchronous machine drives—a review. IEEE Trans. Industr. Electron. 67(7), 5830–5842 (2020). https://doi.org/10. 1109/TIE.2019.2955409
- Benjak, O., Gerling, D.: Review of position estimation methods for IPMSM drives without a position sensor part II: Adaptive methods. In: The XIX International Conference on Electrical Machines—ICEM 2010, Rome, Italy, 2010, pp. 1–6. https://doi. org/10.1109/ICELMACH.2010.5607980
- Wu, X., et al.: Sensorless control of IPMSM equipped with LC sinusoidal filter based on full-order sliding mode observer and feedforward QPLL. IEEE Trans. Power Electron. 39(7), 8072–8085 (2024). https://doi.org/10.1109/TPEL.2024.3390050
- Zuo, Y., et al.: Sensorless control of IPMSM drives based on extended state observer with enhanced position estimation accuracy. IEEE Trans. Power Electron. 40(1), 787–800 (2025). https://doi.org/10.1109/TPEL.2024.3481966
- Shuang, B., Zhu, Z.Q., Wu, X.: Improved cross-coupling effect compensation method for sensorless control of IPMSM with high frequency voltage injection. IEEE Trans. Energy Convers. 37(1), 347–358 (2022). https://doi.org/10.1109/TEC.2021.3093361
- Li, K., Sun, T., Liang, J., Koc, M., Zhou, Y.: Automatic MTPA control for IPMSM drives based on pseudorandomly reversed fixed-frequency sinusoidal signal injection. IEEE Trans. Industr. Electron. 71(7), 6863–6874 (2024). https://doi.org/10.1109/TIE. 2023.3301523
- Yu, Z., Zhang, Y., Feng, Y., Wang, Y., Xu, C.: IPMSM sensorless control technology based on high frequency square-wave injection method. In: Proceedings of SPIE 12965, AOPC 2023: novel technologies and instruments for astronomical imaging and spectroscopy, 1296505 (18 December 2023). https://doi.org/10.1117/ 12.3000610
- Zhang, Z., Shen, A., Li, P., et al.: MTPA-based high-frequency square-wave voltage signal injection strategy for IPMSM control. J. Power Electron. 21, 1461–1472 (2021). https://doi.org/10.1007/ s43236-021-00284-y
- Wang, Z., Yu, K., Li, Y., Gu, M.: Position sensorless control of dual three-phase IPMSM drives with high-frequency square-wave voltage injection. IEEE Trans. Industr. Electron. 70(10), 9925– 9934 (2023). https://doi.org/10.1109/TIE.2022.3222683
- Chen, S., Ding, W., Wu, X., Huo, L., Hu, R., Shi, S.: Sensor-less control of IPMSM drives using high-frequency pulse voltage injection with random pulse sequence for audible noise reduction. IEEE Trans. Power Electron. 38(8), 9395–9408 (2023). https://doi.org/10.1109/TPEL.2023.3266924
- Yoon, Y.-D., Sul, S.-K., Morimoto, S., Ide, K.: High-bandwidth sensorless algorithm for AC machines based on square-wave-type voltage injection. IEEE Trans. Industr. Appl. 47(3), 1361–1370 (2011). https://doi.org/10.1109/TIA.2011.2126552
- Hu, H., Du, J.: Active disturbance rejection control for permanent magnet linear synchronous motor. In: 2021 13th International Symposium on Linear Drives for Industry Applications (LDIA), Wuhan, China, 2021, pp. 1–6. https://doi.org/10.1109/LDIA4 9489.2021.9505994
- Pu, Z., Yuan, R., Yi, J., Tan, X.: A class of adaptive extended state observers for nonlinear disturbed systems. IEEE Trans. Industr. Electron. 62(9), 5858–5869 (2015). https://doi.org/10.1109/TIE. 2015.2448060
- Lin, P., Wu, Z., Liu, K., et al.: A class of linear-nonlinear switching active disturbance rejection speed and current controllers for PMSM. IEEE Trans. Power Electron. 36(12), 14366–14382 (2021)
- Wang, G., Liu, R., Zhao, N., Ding, D., Xu, D.: Enhanced linear ADRC strategy for HF pulse voltage signal injection-based sensorless IPMSM drives. IEEE Trans. Power Electron. 34(1), 514–525 (2019). https://doi.org/10.1109/TPEL.2018.2814056

- Feng, X., Xie, S., Zhang, Z., Chen, Y., et al.: Research on speed loop control of IPMSM based on fuzzy linear active disturbance rejection control. Energy Rep. 8, 804–812 (2022). https://doi.org/ 10.1016/j.egyr.2022.05.258
- Huang, S., Kuang, J., Huang, Q., Huang, K., Gao, J., Liu, T.: IPMSM sensorless control based on fuzzy active-disturbance rejection controller for electric vehicle. In: 2011 International Conference on Power Engineering, Energy and Electrical Drives, Malaga, Spain, 2011, pp. 1–6. https://doi.org/10.1109/PowerEng. 2011.6036495
- Yang, F., Jiang, F., et al.: Complex coefficient active disturbance rejection controller for current harmonics suppression of IPMSM drives. IEEE Trans. Power Electron. 37(9), 10443–10454 (2022). https://doi.org/10.1109/TPEL.2022.3168367
- Xu, J., Wei, Z., Wang, S.: active disturbance rejection repetitive control for current harmonic suppression of PMSM. IEEE Trans. Power Electron. 38(11), 14423–14437 (2023). https://doi.org/10. 1109/TPEL.2023.3307446
- Zhang, Y., Yin, Z., Bai, C., et al.: A rotor position and speed estimation method using an improved linear extended state observer for IPMSM sensorless drives. IEEE Trans. Power Electron. 36(12), 14062–14073 (2021). https://doi.org/10.1109/TPEL.2021. 3085126
- Qu, L., Teng, J.: A linear active disturbance rejection control based sensorless control for IPMSMs considering harmonic current suppression. In: 2022 IEEE Applied Power Electronics Conference and Exposition (APEC), Houston, TX, USA, 2022, pp. 687–692. https://doi.org/10.1109/APEC43599.2022.9773381



Liwei Wang is presently working towards his M.S. degree in the Department of Electrical and Electronic Engineering, The Hong Kong Polytechnic University, Hong Kong Special Administrative Region, China. He is also working as a research assistant in the College of the Electrical Engineering, Sichuan University, Chengdu, China. His current research interests include new energy conversion and control.



Hong Miao received her Ph.D. degree in power electronics from Osaka University, Osaka, Japan, in 2010. Since 1995, she has been with Sichuan University, Chengdu, China. Since 2010, she has been an Associate Professor in the College of the Electrical Engineering, Sichuan University. Her current research interests include the application of power electronics, real-time simulation technology, and power hardware-in-the-loop simulations.

